Nanoscale

PAPER

View Article Online
View Journal | View Issue



Cite this: *Nanoscale*, 2020, **12**, 13086

# Molybdenum carbide and oxycarbide from carbon-supported $MoO_3$ nanosheets: phase evolution and DRM catalytic activity assessed by TEM and *in situ* XANES/XRD methods†

Alexey Kurlov, [a] Xing Huang, *[b] Evgeniya B. Deeva,[a] Paula M. Abdala, [a] Alexey Fedorov *[a] and Christoph R. Müller *[a]

Received 12th April 2020,
Accepted 8th June 2020

DOI: 10.1039/d0nr02908d

rsc.li/nanoscale

Molybdenum carbide (β-$Mo_2C$) supported on carbon spheres was prepared *via* a carbothermal hydrogen reduction (CHR) method from delaminated nanosheets of molybdenum(VI) oxide (*d*-$MoO_3$/C). The carburization process was followed by combined *in situ* XANES/XRD analysis revealing the formation of molybdenum oxycarbide $Mo_2C_xO_y$ as an intermediate phase during the transformation of *d*-$MoO_3$/C to β-$Mo_2C$/C. It was found that $Mo_2C_xO_y$ could not be completely carburized to β-$Mo_2C$ under a He atmosphere at 750 °C, instead a reduction in $H_2$ is required. The β-$Mo_2C$/C obtained showed activity and stability for the dry reforming of methane at 800 °C and 8 bar. *In situ* XANES/XRD evaluation of the catalyst under DRM reaction conditions combined with high resolution TEM analysis revealed the evolution of β-$Mo_2C$/C to $Mo_2C_xO_y$/C. Notably, the gradual oxidation of β-$Mo_2C$/C to $Mo_2C_xO_y$/C correlates directly with the increased activity of the competing reverse water gas shift reaction.



## Introduction

Since the 1970s reports on the noble-metal-like catalytic activity of $Mo_2C$[1] and WC,[2] transition metal carbides have remained in the focus of the catalysis community.[3–11] For instance, molybdenum carbide has been studied as a catalyst for various heterogeneous reactions including methane reforming,[12,13] methane dehydroaromatization,[14,15] water gas shift,[16–18] and deoxygenation reactions.[19–22] The dry reforming of methane (DRM, eqn (1)) is a particularly relevant reaction because it allows producing synthesis gas from the two main greenhouse gases, $CH_4$ and $CO_2$, although it requires high temperatures for reaching high conversions (typically, 800 °C and above).[23] However, $Mo_2C$ catalyzes also the reverse water gas shift reaction (RWGS, eqn (2)),[24–26] which can occur in parallel with the DRM reaction consuming the hydrogen produced, resulting in a decreased $H_2$/CO ratio of the produced syngas and the formation of steam.[23,27,28] Currently, it remains unclear if the active sites for DRM and RWGS in $Mo_2C$ catalyst are identical.

$$CH_4 + CO_2 \leftrightarrow 2CO + 2H_2 \quad \Delta H_{298\ K} = +247\ \text{kJ mol}^{-1} \quad (1)$$

$$CO_2 + H_2 \leftrightarrow CO + H_2O \quad \Delta H_{298\ K} = +41\ \text{kJ mol}^{-1} \quad (2)$$

The oxophilicity of $Mo_2C$ and, ultimately, its instability against oxidation to $MoO_2$ [12,29,30] in $CO_2$-rich feeds at high operating temperatures make the DRM challenging for $Mo_2C$-based catalysts.[12,13,30–33] To attenuate this oxidative deactivation, DRM is often conducted at elevated pressure (2–10 bar) and/or with $CH_4$-rich feeds.[12,29,31,34] Those reports have indicated that a pristine $Mo_2C$ surface evolves to a molybdenum oxycarbide surface layer or a phase ($Mo_2C_xO_y$), which plays a key role in both the DRM and RWGS reactions. It is also known that the oxygen coverage of the molybdenum carbide surface influences substantially its activity and selectivity, for instance in $CO_2$-assisted propane dehydrogenation.[35]

Supported $Mo_2C$-based catalysts are usually prepared by a so-called temperature programed reduction (TPR) method, *i.e.* a gas–solid reduction of molybdenum oxide (or ammonia molybdate precursor) by a mixture of $H_2$ and a carbonaceous gas such as $CH_4$ or $C_2H_6$.[12,20,21,24,36] However, this procedure may also deposit passivating carbon on the catalytically active carbide surface.[36] Alternatively, a carbothermal hydrogen reduction (CHR) method involving a reaction between solid

[a]*ETH Zürich, Department of Mechanical and Process Engineering, Leonhardstrasse 21, CH 8092 Zürich, Switzerland. E-mail: fedoroal@ethz.ch, muelchri@ethz.ch*
[b]*ETH Zürich, The Scientific Center for Optical and Electron Microscopy (ScopeM), Otto-Stern-Weg 3, CH 8093 Zürich, Switzerland. E-mail: xing.huang@scopem.ethz.ch*
†Electronic supplementary information (ESI) available. See DOI: 10.1039/d0nr02908d

carbon (or a carbon containing material) and molybdenum oxide under reducing ($H_2$) or inert atmosphere can be exploited.[37–39] The relatively low carburization temperatures (typically, <800 °C) and the absence of carbonaceous gases favour the production of high surface area nanostructured $Mo_2C$, which is beneficial for catalytic applications.

Here, we studied the CHR reaction of two dimensional delaminated $MoO_3$ nanosheets (*d*-$MoO_3$) supported on carbon spheres, which served as carbon source for carburization and also provided a suitable morphological and phase contrast for transmission electron microscopy. Combination of *in situ* XANES/XRD analysis[18,40,41] and high resolution TEM revealed that $Mo_2C_xO_y$ is an intermediate phase during the carbothermal CHR reaction of *d*-$MoO_3$/C to β-$Mo_2C$/C. Additionally, we demonstrate that under DRM conditions, β-$Mo_2C$/C evolves into $Mo_2C_xO_y$/C, which is found in active catalyst. Detection of the $H_2O$ produced during the *in situ* XANES/XRD (DRM conditions) experiments allowed us to link the oxidation of β-$Mo_2C$/C to the emergence of the competing RWGS reaction. High resolution TEM of the active catalyst demonstrates two different morphologies, *i.e.* aggregates of nanoplatelets and nanorods, corresponding to β-$Mo_2C$ and $Mo_2C_xO_y$ structures, respectively.

## Experimental section

### Materials

The orthorhombic α-$MoO_3$ nanobelts were synthesized by a reported hydrothermal method using ammonium heptamolybdate tetrahydrate (AHM, Sigma-Aldrich, 99.98% trace metals basis) and nitric acid (70%, Sigma-Aldrich, ACS reagent grade).[42] In a standard experiment, the pH of AHM (1 g) solution in deionized (DI) water (20 mL) was adjusted to 1 by the dropwise addition of $HNO_3$ (*ca.* 5 mL). The reaction mixture was then kept at 180 °C for 24 h in a Teflon-lined autoclave (45 mL). The obtained material was washed with DI water until a pH of *ca.* 7 was reached and subsequently dried at 100 °C.

*d*-$MoO_3$ nanosheets were synthesized according to a reported method.[43] The orthorhombic α-$MoO_3$ (1 g) was ground in an agate mortar with acetonitrile (0.2 mL, Sigma-Aldrich, ACS reagent, ≥99.5% purity) and the resulting material was dispersed by sonication in 50% aqueous ethanol (15 mL) for 2 h. After sonication, the suspension was centrifuged (8000 rpm, 30 min) and the supernatant containing the dissolved *d*-$MoO_3$ nanosheets was collected and used for impregnation onto carbon spheres.

Carbon spheres were synthesized *via* a hydrothermal method from xylose (Sigma-Aldrich, ≥99% purity) in water.[44,45] Xylose (6 g) was dissolved in DI water (15 mL) and the mixture was kept at 180 °C for 20 h in a Teflon-lined autoclave (45 mL).

*d*-$MoO_3$/C material was obtained *via* wet impregnation of the supernatant solution of *d*-$MoO_3$ (*ca.* 1.5 mg $mL^{-1}$ by the thermogravimetric analysis) onto carbon spheres. The following treatment was applied: annealing of *d*-$MoO_3$/C in $N_2$ (800 °C, 1.5 h, 5 °C $min^{-1}$) followed by annealing in 10 vol% $H_2$ in $N_2$ (30 min, 800 °C) giving ultimately β-$Mo_2C$/C.

### Characterization

*Ex situ* X-ray powder diffraction (XRD) data were collected on a PANalytical Empyrean X-ray diffractometer equipped with a Bragg–Brentano HD mirror and operated at 45 kV and 40 mA using CuKα radiation ($\lambda$ = 1.5418 nm). The materials were examined within the $2\theta$ range of 5–90° using a step size of 0.0167°. The scan time per step was 3 s. Thermogravimetric analysis (TGA) experiments were performed in a Mettler Toledo TGA/DSC 3 instrument. Typically, 750 μL of a colloidal solution of *d*-$MoO_3$ was placed in a sapphire crucible (900 μL) that was heated to 80 °C (5 °C $min^{-1}$) and kept for 1 h. Inductively coupled plasma atomic emission spectroscopy (ICP-AES) analysis was performed by the Mikroanalytisches Labor Pascher (Remagen, Germany). Scanning electron microscopy (SEM) was performed on a Zeiss LEO Gemini 1530 microscope. All electron microscopy images were taken at an acceleration voltage of 5 kV. Prior to imaging the materials were coated with a *ca.* 2 nm conductive layer of platinum.

Transmission electron microscopy (TEM) samples were prepared by dry-deposition of the sample powders onto Cu TEM grids covered with a thin holey carbon layer. TEM, high resolution TEM (HR-TEM) and high angle annular dark field scanning TEM (HAADF-STEM) images of the samples were taken by an aberration-corrected JEOL JEM-ARM 300F GrandARM transmission electron microscope operated at 300 kV. The energy-dispersive X-ray spectroscopy (EDX) elemental mapping was performed using dual silicon drift EDX detectors with a total detection area of 200 $mm^2$. The electron energy loss (EELS) spectra were recorded in dual EELS mode by a GIF Quantum ER System (Model 965) that is attached to the TEM.

Combined X-ray absorption spectroscopy (XAS) and powder diffraction (XRD) experiments were performed at the Swiss-Norwegian Beamlines (SNBL, BM31) at the European Synchrotron Radiation Facility (ESRF, Grenoble, France). XAS spectra were collected at the Mo K-edge using a double-crystal Si (111) monochromator with continuous scanning in transmission mode. XRD data were collected using a DEXELA-PerkinElmer 2923 CMOS pixel detector[46] and a Si (111) channel-cut monochromator set at a wavelength of $\lambda$ = 0.5 Å. The *in situ* dry reforming of methane (DRM) experiment was performed in a quartz capillary reactor.[47] Calibration of the XAS data was based on Mo foil set at 20 000.0 eV. In a typical XAS experiment *ca.* 2 mg of *d*-$MoO_3$/C was placed between two quartz wool plugs in a capillary reactor (outer diameter 1.5 mm, wall thickness 0.1 mm). The carburization step was performed in pure He in the temperature range from 50 to 750 °C (5 mL $min^{-1}$, *ca.* 4.5 °C $min^{-1}$); a final annealing was performed in 50 vol% $H_2$ in He (750 °C, 10 mL $min^{-1}$, *ca.* 20 min). DRM tests were performed at 8 bar ($CH_4 : CO_2 : He$ = 4 : 3 : 3) with the total flow rate varying in the range 1.75–3.5 mL $min^{-1}$ (space velocity (SV) of *ca.* 3500–7000 L $g_{Mo}^{-1}$ $h^{-1}$; catalyst weight/volume flow rate (W/F) ratio of *ca.* 0.5–1 ms $g_{Mo}$ $mL^{-1}$) at 730 °C. The composition of the outlet

gases was followed online by a mass spectrometer (MS). *Ex situ* XAS data were collected from pellets of reference materials with an optimized amount of sample mixed with cellulose. Activated materials were handled in a $N_2$-filled glove box to prepare specimen for XAS analysis in air-tight sealed Al bags. XAS data were processed using the Athena software (Demeter 0.9.25 software package).[48] *In situ* time resolved XANES data were analyzed using a Multivariate Curve Resolution-Alternating Least Squares (MCR-ALS) method.[40,49] MCR-ALS analysis was performed with a MATLAB software package using the multivariate curve resolution toolbox.[50] The experimental spectra were analyzed in the 19 950–20 100 eV energy range. The number of components characterizing the whole XANES spectra dataset was determined using principal component analysis (PCA). Non-negative constraints for both the phase concentration and spectra profiles as well as cumulative concentration profile closure to 1 were applied in the analysis.[49] The MCR-ALS routine was regarded successful when the convergence criterion fell below 0.1%.

### Catalytic testing

The laboratory DRM tests were carried out in a metal fixed-bed reactor (Hastelloy X, 8 mm inner diameter) at 8 bar. In a typical experiment, 75 mg of *d*-$MoO_3$/C was placed in between two quartz wool plugs. Prior to the catalytic tests, *d*-$MoO_3$/C was transformed *in situ* into β-$Mo_2C$/C by thermal treatment in (1) $N_2$ (800 °C, 1.5 h, 20 mL $min^{-1}$, 5 °C $min^{-1}$) followed by (2) 10 vol% $H_2$ in $N_2$ (800 °C, 30 min, 20 mL $min^{-1}$) at atmospheric pressure. After this pretreatment, the pressure was increased to 8 bar ($N_2$) and the DRM feed was introduced ($CH_4 : CO_2 : N_2 = 4 : 3 : 3$, a total flow rate was 10 mL $min^{-1}$, SV *ca.* 550 L $g_{Mo}^{-1}$ $h^{-1}$, W/F *ca.* 6.5 ms $g_{Mo}$ $mL^{-1}$, 800 °C, 8 bar). The composition of the off-gas was analyzed *via* a gas chromatograph (GC, PerkinElmer Clarus 580) equipped with a thermal conductivity detector (TCD).

## Results and discussion

Orthorhombic α-$MoO_3$ nanobelts were synthesized *via* a reported route.[42] The nanobelt morphology of α-$MoO_3$ was confirmed by scanning electron microscopy (SEM, Fig. S1†) and phase purity by X-ray powder diffraction (XRD) analysis (space group *Pbnm*, Fig. S2†). Note that increasing the Mo concentration in the hydrothermal synthesis from 0.56 to 2 mol $L^{-1}$ yields a hexagonal polymorph *h*-$MoO_3$ (space group $P6_3/m$, Fig. S3†). Sonication of grinded α-$MoO_3$ and its dispersion in 50% aqueous ethanol yielded, after centrifugation, a transparent colloidal solution of delaminated $MoO_3$ films (*d*-$MoO_3$). Transmission electron microscopy (TEM) imaging of a dried aliquot of this solution revealed a few-layer-thin nanosheets of *d*-$MoO_3$ (Fig. S4†). High resolution TEM (HR-TEM) images show lattice fringes separated by 3.72 Å, which is characteristic for the distance of the (1 1 0) planes in α-$MoO_3$ (Fig. S4†). The wet impregnation of carbon spheres (Fig. S5†) with the colloidal solution of *d*-$MoO_3$ nanosheets (*ca.* 1.5 mg $mL^{-1}$ by thermogravimetric analysis, Fig. S6†) yielded, after drying at 100 °C, *d*-$MoO_3$/C (1.49 wt% Mo by elemental analysis). High angle annular dark field scanning TEM (HAADF-STEM) imaging of *d*-$MoO_3$/C shows carbon spheres (light contrast) covered by a Mo-rich phase (heavier contrast) that segregates as poorly crystalline halo-like patterns around the carbon spheres (Fig. 1b–d and S7†). We also observed small poorly ordered crystalline clusters imbedded in the amorphous matrix of carbon spheres, as shown in Fig. 1d and S7.† Energy-dispersive X-ray spectroscopy (EDX) mapping indicates that the Mo-rich phase contains both Mo and O, consistent with *d*-$MoO_3$, as well as C from, possibly, bound acetonitrile/ethanol solvent molecules (Fig. S8†). In agreement with EDX, electron energy loss spectroscopy (EELS) analysis indicates that the material contains C, O, and Mo (Fig. S9†). According to the shape and energy position of the O K-edge peak (*ca.* 530 eV), Mo atoms have an oxidation state between +4 and +6 (Fig. S10†).[51,52] The partial reduction of Mo +6 states is likely due to the electron beam reduction during the acquisition of EELS data, consistent with the previous data.[51]

Annealing of *d*-$MoO_3$/C at 800 °C in $N_2$ (1.5 h) followed by an additional annealing step in 10 vol% $H_2$ (800 °C, 30 min) gave $Mo_2C$/C. STEM imaging of this material, after exposure of the specimen to air during sample transfer, reveals crystalline nanorods of *ca.* 100–500 nm in length decorating the surface of carbon spheres (Fig. 1f). Additionally, crystalline agglomerates (Fig. 1g and h) and core/shell nanoparticles (Fig. 1i) were found on the surface of the carbon spheres. HAADF-STEM images uncover that the core/shell structures have a crystalline core and an amorphous shell (Fig. 1i). EELS analysis performed on all observed morphologies demonstrates a shift of the Mo $M_{2,3}$ edge to a lower energy when compared to *d*-$MoO_3$/C, which indicates a more reduced Mo. However, the oxidization state of Mo is between +2 to +4 (Fig. S11†). Furthermore, EDX mapping confirms the oxidized state of Mo, revealing that all structures contain Mo, C and O (Fig. 1e). These results indicate that an oxidation of molybdenum carbide took place when exposing the activated reduced material to ambient air during sample transfer, consistent with the high reactivity of the activated, highly oxophilic $Mo_2C$ surface.[53]

To obtain information about the state of the annealed material at the specific temperatures and gas atmospheres, we turned to *in situ* experimentation and followed the CHR process (*d*-$MoO_3$/C → β-$Mo_2C$/C) by a combined *in situ* XANES/XRD experiment.[18,40,41] The XANES spectra were collected at the Mo K-edge during annealing of *d*-$MoO_3$/C from 50 to 750 °C (highest attainable temperature of the set up) under He and 50% $H_2$/He at 750 °C (total flow rates of 5 and 10 mL $min^{-1}$, respectively), while XRD patterns were collected at 50, 400 and 750 °C during the same experiment. For the latter temperature, data were collected under a flow of pure helium or 50% $H_2$/He. The XRD pattern collected at 50 °C contains no Bragg peaks and shows a dominant amorphous halo due to the C phase, confirming the low crystallinity of the *d*-$MoO_3$/C material as observed by TEM (Fig. 2a and 1d). At 400 °C, Bragg peaks corresponding to the $MoO_2$ phase (distorted rutile type

 

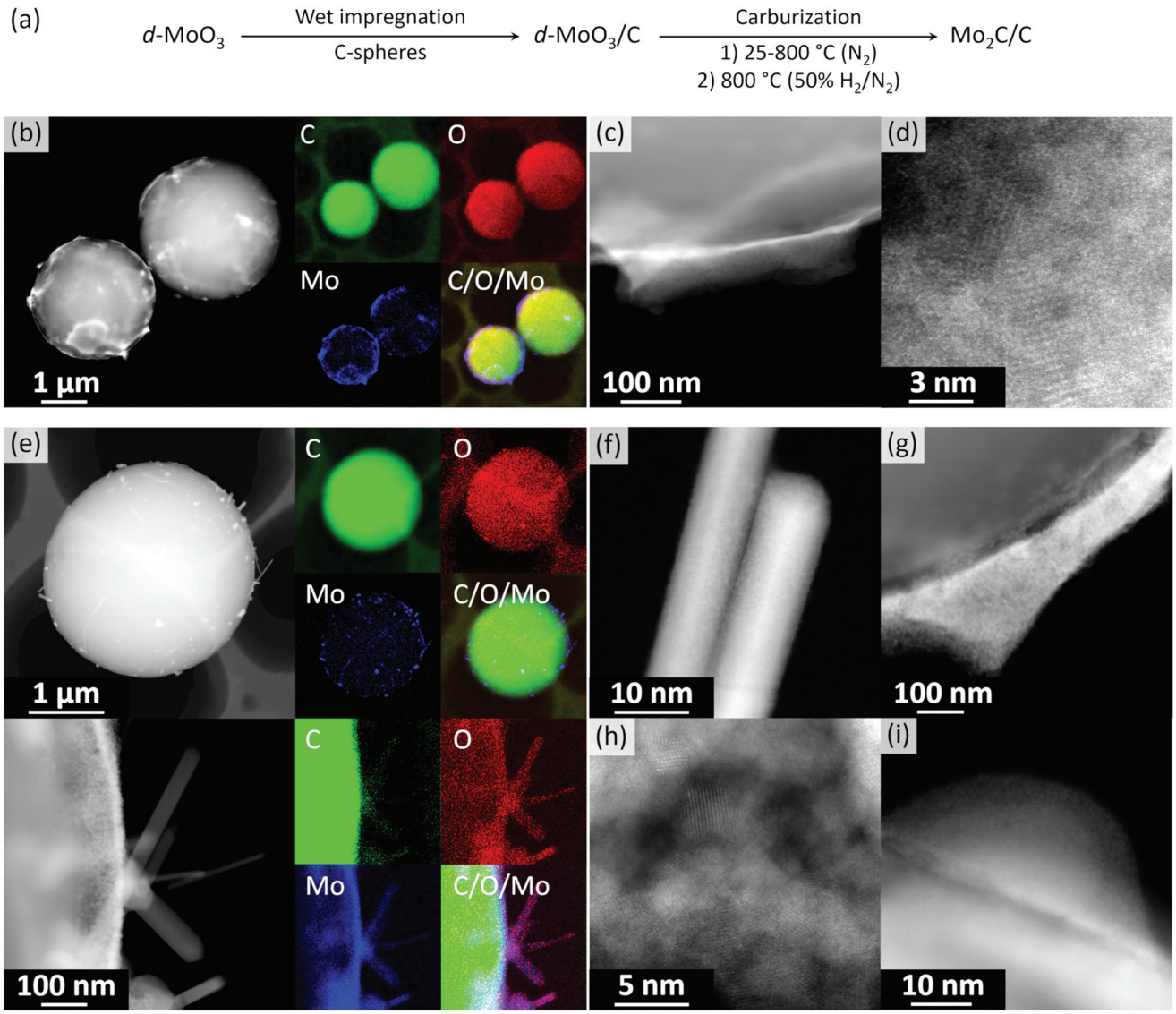


**Fig. 1** (a) Synthesis of β-$Mo_2C$/C from delaminated $MoO_3$ films; (b) HAADF-STEM images and EDX maps of *d*-$MoO_3$/C; (c) and (d) HR-STEM images of *d*-$MoO_3$/C; (e) HAADF-STEM images and EDX maps of β-$Mo_2C$/C; and (f)–(i) HR-STEM images of different morphologies decorating the surface of carbon spheres in β-$Mo_2C$/C.

structure, space group $P2_1/c$) appear, indicating a reduction of *d*-$MoO_3$ to $MoO_2$ by the carbon spheres (reducing agent), accompanied by the crystallization of $MoO_2$ (Fig. 2a). Interestingly, while at 750 °C under a He atmosphere only reflections of $MoO_2$ are present, flowing $H_2$ through the specimen immediately reduced it to β-$Mo_2C$ (Fig. 2a). Our *in situ* XRD results agree well with previous studies that have identified $MoO_2$ as an intermediate phase during the carburization of $MoO_3$ to $Mo_2C$, both *via* TPR[25,54] and CHR[39,55,56] routes. In addition, it was also reported that annealing of carbon-supported AHM in pure He at 800 °C for 2 h does not lead to its complete carburization, giving a mixture of $MoO_2$ and β-$Mo_2C$.[56]

The *in situ* XANES data collected during annealing of *d*-$MoO_3$/C indicates clearly a gradual reduction of $Mo^{6+}$ to $Mo^{4+}$ when heating under He to 750 °C and the formation of β-$Mo_2C$, upon switching to 50 vol% $H_2$/He, as confirmed by a shift of the Mo K edge energies from 20 016.3 (at room temperature) to, respectively 20 011.6 and 20 000.6 eV (without and with co-feed $H_2$ at 750 °C; Fig. 2b).[18] Two notable changes are observed in the *in situ* XANES spectra. The first change occurs at *ca.* 360 °C and is associated with the disappearance of the characteristic pre-edge feature, typical for molybdenum in a non-centrosymmetric environment (Fig. 2b, inset),[57,58] that can be explained by the reduction/transformation of *d*-$MoO_3$ to $MoO_2$. From 360 °C to 750 °C (heating up in He), a slight shift of the Mo K-edge position towards lower energies is observed, consistent with a partial reduction. The second change occurs immediately after introducing $H_2$ at 750 °C and is associated with a prominent shift of the Mo K-edge position

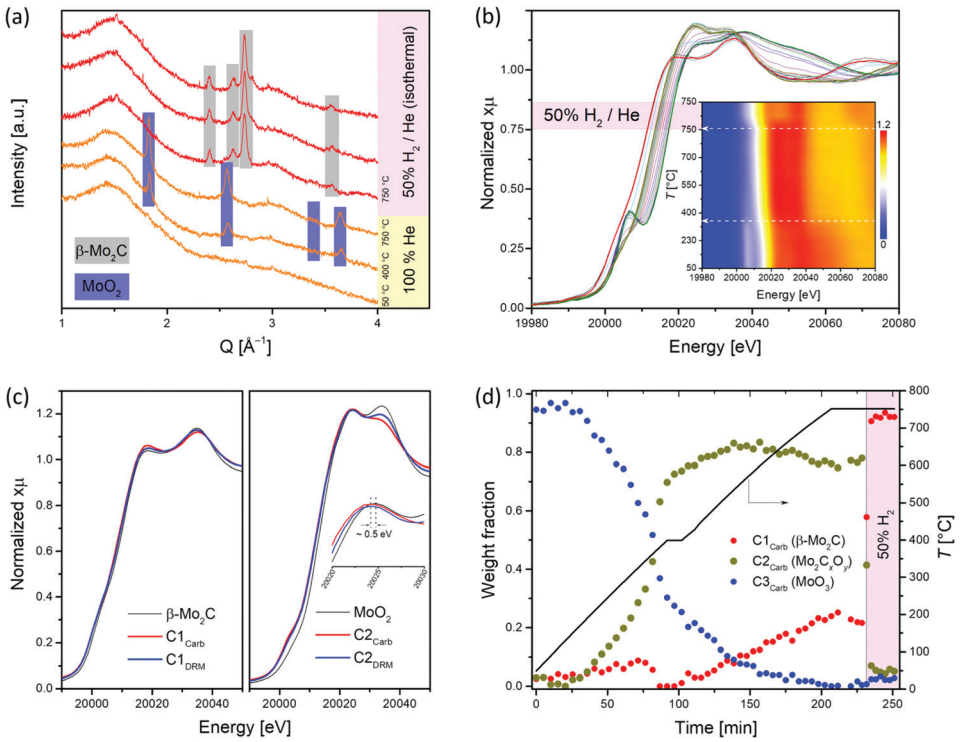


**Fig. 2** *In situ* carburization of *d*-$MoO_3$/C under He and $H_2$ as followed by (a) XRD ($Q = 4\pi \sin(\theta)/\lambda$) and (b) Mo K-edge XANES; the inset shows the evolution of the pre-edge and edge features with increasing temperature. (c) Comparison of the extracted C1 and C2 components spectra from the MCR-ALS analysis performed during the carburization of *d*-$MoO_3$/C (labelled Carb) to β-$Mo_2C$/C and during the dry reforming of methane (labelled DRM, *vide infra*) along with the references β-$Mo_2C$ and $MoO_2$. (d) Phase evolution during the carburization process according to MCR-ALS of the XANES data.

from 20 011.6 to 20 000.6 eV, highlighting a further reduction of the Mo phase. In agreement with the *in situ* XRD data, the XANES spectrum of the final phase corresponds to the reference spectrum of β-$Mo_2C$.

Further analysis of the *in situ* XANES data *via* principal component analysis (PCA) indicates the presence of three components during the annealing of *d*-$MoO_3$/C (Fig. S12†). Using the information of the presence of three phases, MCR-ALS analysis was performed to extract the three components spectra that reproduce the full data set (Fig. S13†). Comparison of the obtained spectra with the available references revealed that the spectrum of the component $C1_{Carb}$ is identical to that of β-$Mo_2C$ (Fig. 2c). The spectrum of component $C2_{Carb}$ resembles that of $MoO_2$ except that the edge and the white line feature are shifted to a lower energy (and the shape of the white line is slightly different), indicating overall a reduced Mo oxidation state compared to $Mo^{4+}$, *i.e.* an oxidation state between $MoO_2$ and $Mo_2C$ (Fig. 2c). This finding suggests assigning the $C2_{Carb}$ component to molybdenum oxycarbide ($Mo_2C_xO_y$). Combining this new insight with XRD analysis, we speculate that the $Mo_2C_xO_y$ phase may be formed due to the incorporation of C into the $MoO_2$ lattice or surface layers during annealing, thus retaining the bulk structure of $MoO_2$ (distorted rutile type structure, space group $P2_1/c$). The formation of such a $MoO_2/Mo_2C_xO_y$ phase is in a good agreement with a previous report indicating that $MoO_2$ can coexist with oxycarbide phases.[59] For brevity, we will refer to the $MoO_2/Mo_2C_xO_y$ phase below as $Mo_2C_xO_y$. Notably, the shape of the obtained XANES spectra of the $C2_{Carb}$ component resembles a recently reported molybdenum oxycarbide $Mo_2C_xO_y$, although here, the Mo K-edge is shifted to lower energies indicating a more reduced Mo state, probably due to the higher C content in the oxycarbide.[60] Lastly, the edge position and the oscillation profile of component $C3_{Carb}$ is similar to that of $MoO_3$, which allows ascribing $C3_{Carb}$ to $MoO_3$. The changes of weight fractions of the $C1_{Carb}$–$C3_{Carb}$ components with annealing is presented in Fig. 2d. $Mo_2C_xO_y$ that is formed *via* the reduction of $MoO_3$ by the carbon of the spheres, starts to appear at *ca.* 200 °C and reaches an asymptotic level of *ca.* 75–80% at 400 °C (Fig. 2d). Surprisingly, MCR indicates that the molybdenum carbide phase appears already at *ca.* 400 °C. This has not been observed in previous carburization studies of supported Mo oxides and is explained by the use of a carbon support as the carburizing agent in place of the traditionally used $CH_4/H_2$ carburizing gas mixture and thin sheets of *d*-$MoO_3$. The fraction of $MoO_3$ reduces continuously from *ca.* 170 °C until it disappears at 750 °C. At this stage $Mo_2C_xO_y$ and $Mo_2C$ coexist in fraction of 75% and 25%, respectively (Fig. 2d). However, as discussed above, a complete carburization by the internal carbon source could not be accomplished

at 750 °C in He. To attain the complete conversion of the remaining $Mo_2C_xO_y$ to β-$Mo_2C$, a gas containing 50 vol% $H_2$ in He was passed through the reactor at 750 °C. Under such conditions the remaining $Mo_2C_xO_y$ was immediately carburized to β-$Mo_2C$ according to MCR analysis (Fig. 2d).

To summarize, although MCR-ALS analysis reveals a coexistance of $Mo_2C_xO_y$ and β-$Mo_2C$ at 750 °C in He, *in situ* XRD data showed only peaks corresponding to distorted rutile type $MoO_2$. This observation can be explained by (i) the amorphous nature of the molybdenum oxycarbide phase and/or (ii) the incorporation of variable amounts of carbon into the $MoO_2$ phase, forming effectively the $Mo_2C_xO_y$ phase with a reduced Mo oxidation state (and the corresponding Mo K-edge position), yet maintaining the same crystal structure as $MoO_2$.

Next, we optimized the DRM conditions to obtain a stable catalytic performance of β-$Mo_2C$/C. The condition identified is a pressure of 8 bar at 800 °C and a $CH_4$-rich feed, *i.e.* $CH_4 : CO_2 : N_2 = 4 : 3 : 3$ (Fig. 3a). In particular, under this condition no considerable deactivation was observed over 8 h. The space time yield (STY) of CO was 0.22 mol(CO) $mol(Mo)^{-1}$ $s^{-1}$ while the methane conversion rate was 0.11 mol($CH_4$) mol $(Mo)^{-1}$ $s^{-1}$ (X($CH_4$) was *ca.* 45%, Fig. 3b). However, the obtained $H_2$/CO ratio was *ca.* 0.7, which indicates that the RWGS and DRM reactions compete under these conditions.

To identify the active state and to follow the structural evolution of the β-$Mo_2C$/C catalyst under DRM conditions, an *in situ* XANES/XRD experiment was carried out in a capillary reactor. After the carburization pre-treatment, the feed was switched to DRM conditions ($CH_4 : CO_2 = 4 : 3$ at 8 bar and 730 °C) while analyzing the composition of the outlet gas by MS. Note that due to the heater limitation, the actual temperature in our catalytic *in situ* XANES/XRD experiment was 730 °C, instead of 800 °C as in the laboratory experiment, yet qualitatively similar results can be expected at those temperatures (Fig. 3c and d). Laboratory and capillary synchrotron DRM experiments differ also in catalyst weight/volume flow rate (W/F) ratio, which were W/F = 6.5 and 1 ms $g_{Mo}$ $mL^{-1}$, respectively. PCA analysis indicates that two components are necessary to account for changes of XANES spectra with time on stream (TOS, Fig. S12†). MCR-ALS analysis of the *in situ* XANES data yielded the XANES spectra for these two components, *i.e.* $C1_{DRM}$ and $C2_{DRM}$ (Fig. S13†). Comparison of the calculated spectra with references and the components obtained in the carburization MCR-ALS analysis, identified them as β-$Mo_2C$ and $Mo_2C_xO_y$, respectively (Fig. 2c and S13†). Notably, the spectrum of the component $C1_{DRM}$, identified as β-$Mo_2C$, is identical to the spectrum of the component $C1_{Carb}$ obtained for the carburization process (Fig. 2c). Interestingly, while the shape and edge position of the spectrum of $C2_{DRM}$ ($Mo_2C_xO_y$) is very similar to $C2_{Carb}$, it bears a notable difference in the intensities of the white line features (Fig. 2c). This can probably be explained by the different C content and/or C distribution within the oxycarbide, formed by incorporation of oxygen atoms into β-$Mo_2C$ (DRM conditions) or by incorporation of carbon atoms into $MoO_2$ (CHR conditions). No changes in XANES spectra and XRD data of β-$Mo_2C$ occur during the first 30–40 min TOS (Fig. 3c and d). Note that the products CO and $H_2$ of the DRM reaction are detected by MS during the entire experiment (Fig. S14†). After this initial period, a shift of the Mo K-edge position to higher energies sets in, indicating the gradual oxidation of β-$Mo_2C$. After *ca.* 1 h of TOS, β-$Mo_2C$ was transformed to $Mo_2C_xO_y$ according to the concentration profiles obtained by MCR analysis (Fig. 3c). Consistent with XANES data, the XRD peaks corresponding to $MoO_2$ (or $Mo_2C_xO_y$) appear after *ca.* 40 min of TOS with a simultaneous reduction of the intensities of the peaks due to β-$Mo_2C$ (Fig. 3d). After 50 min TOS, the $MoO_2$ peaks reach their maximal intensities and only a low intensity (1 2 1) peak of β-$Mo_2C$ ($Q$ = 2.74 $Å^{-1}$) could be detected at this time. Interestingly, the MS data reveals an increase of the $H_2O$ signal starting from TOS = 45 min, arising from the competing RWGS reaction. The increase in the MS $H_2O$ signal coincides with the beginning of the oxidation of β-$Mo_2C$ observed by XANES and XRD (Fig. S14†). This result suggests that the RWGS reaction is favoured on a more oxygen-rich $Mo_2C_xO_y$ phase.

Flowing pure $CH_4$ for 1 h through the reacted catalyst after 130 min TOS does not lead to a re-carburization, leaving the catalyst composition unchanged according to the XANES data (Fig. S15†).

We have also investigated by TEM the active state of the $Mo_2C$/C catalyst, *i.e.* the material recovered after cooling down the working catalyst to room temperature in $N_2$ after 480 min TOS ($Mo_2C/C_{TOS480}$) at the stable performance stage (Fig. 3d). The specimen was transferred in ambient air before the TEM analysis. $Mo_2C/C_{TOS480}$ features aggregates of nanoplates and nanorods as the two main morphologies (Fig. 3d and S16†). We observe that the crystallinity of the material surface layer (for both morphologies) is lower compared to the crystallinity of the bulk structure (Fig. S17†). Based on the EELS data, the Mo $M_{2,3}$ edges position shows that the molybdenum oxidation state is below +4. Interestingly, the maximum of the Mo $M_3$ edge of $Mo_2C/C_{TOS480}$ is found at a lower energy compared to that of $Mo_2C$/C (395.5 eV and 397.5 eV, respectively, Fig. S11†), although both materials were exposed to ambient air during the transfer. This difference might be owing to the oxidation of β-$Mo_2C$ during the DRM reaction, which enriches the catalyst surface layers with O, thereby preventing a further oxidation in air at room temperature. For both morphologies, the EDX mapping shows the presence of Mo, C and O elements, however, a higher oxygen to molybdenum ratio is observed in the nanorods compared to the nanoparticles (Fig. S18†). Additionally, a higher oxygen content is observed in the surface layer compared to the bulk structure for both morphologies (Fig. S19†), in line with the presence of an oxycarbidic layer. The structural analysis of a plate-like nanoparticle by HR-TEM reveals that its crystal structure matches that of the orthorhombic $Mo_2C$ (Fig. 3e, top). In particular, the observed structure fits perfectly the [4 3 2] zone axis of β-$Mo_2C$ (*Pbcn*). In contrast, the nanorod structure does not correspond to β-$Mo_2C$ and it fits neither to $MoO_3$ or $MoO_2$ with a distorted rutile

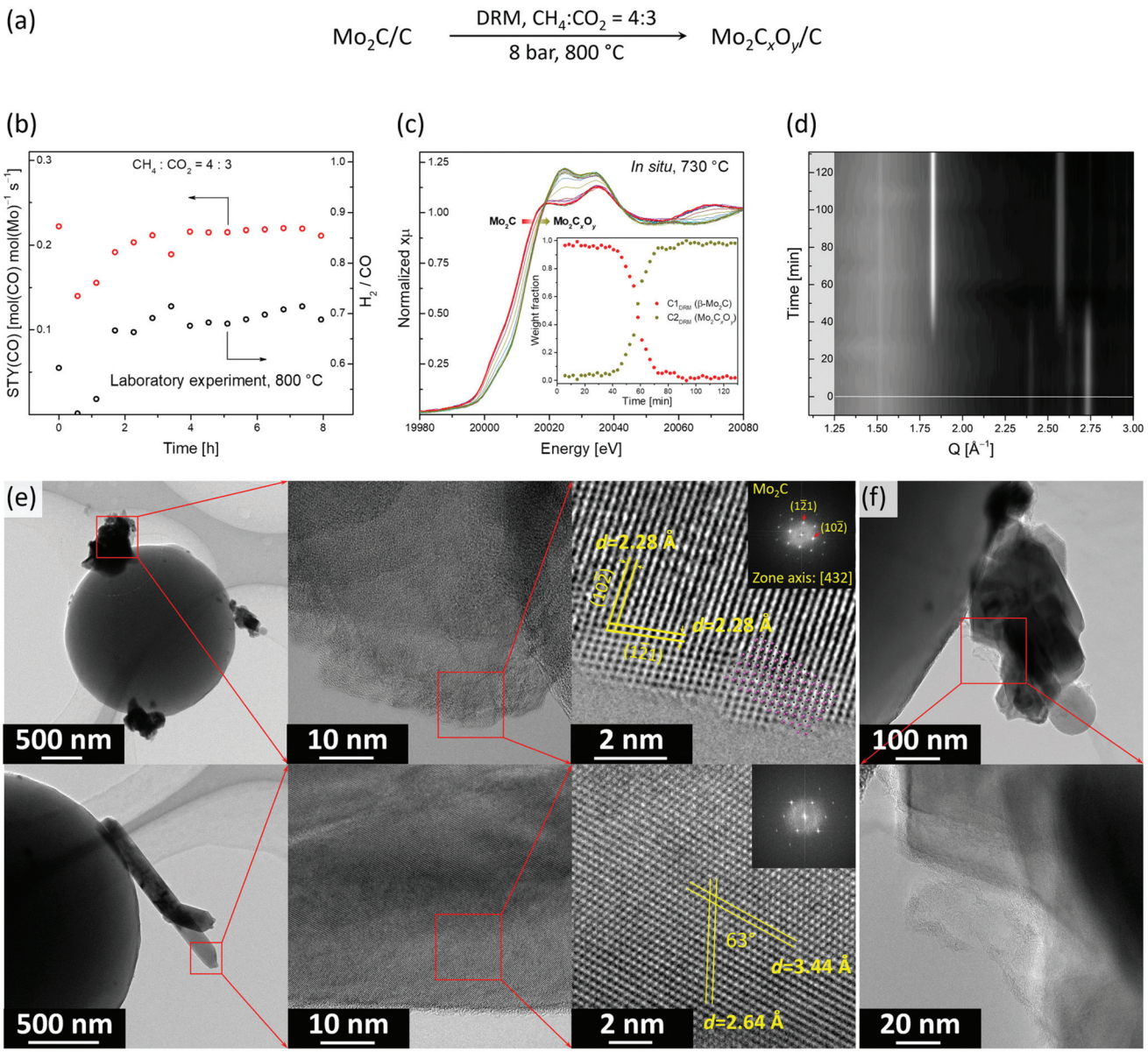


**Fig. 3** (a) Schematic of the experimental conditions during the DRM experiment; (b) catalytic performance of β-$Mo_2C$/C in DRM (laboratory scale reactor, 800 °C, 8 bar, SV = 550 L $g_{Mo}^{-1}$ $h^{-1}$); DRM experiment followed by (c) Mo K-edge XANES, where the inset shows the phase evolution according to MCR-ALS, and (d) XRD ($Q = 4\pi \sin(\theta)/\lambda$) (capillary reactor, 730 °C, 8 bar, SV = 3500 L $g_{Mo}^{-1}$ $h^{-1}$); (e) TEM and HR-TEM images of the spent $Mo_2C_xO_y$/C catalyst revealing two different morphologies, *i.e.* aggregates of nanoplates (top) and nanorods (bottom); (f) TEM images of amorphous carbon deposited on the active $Mo_2C_xO_y$/C catalyst.

structure (Fig. S20†). This observation combined with a high O content, in addition to the simultaneous presence of Mo and C elements in the EDX maps, allows us to attribute the nanorods to a crystalline oxycarbidic phase $Mo_2C_xO_y$. Additionally, amorphous carbon was found attached to the surface of $Mo_2C/C_{TOS480}$ (Fig. 3e). The origin of the carbon observed can be either the partial degradation of the carbon spheres support or catalyst coking under reaction conditions. However the latter is unlikely due to the low coking rate of carbide based catalysts.[12] Noteworthy, the TEM analysis of $Mo_2C/C_{TOS480}$ reveals no presence of $MoO_2$ proving the high stability of $Mo_2C_xO_y$ towards oxidation under operating conditions.

## Conclusions

We have shown that delaminated $MoO_3$ nanosheets dispersed on carbon spheres, are carburized only partially by annealing in an inert gas and require $H_2$ to form β-$Mo_2C$/C quantitatively. The carburized material shows a stable performance in the DRM reaction at an elevated pressure of 8 bar. The combi-

nation of advanced *in situ* XANES/XRD analysis and TEM characterization allowed us to attribute a combination of β-$Mo_2C$ and $Mo_2C_xO_y$ to the active state of the catalyst. In addition, the higher oxidation states of β-$Mo_2C$/$Mo_2C_xO_y$ catalyst correlate with higher rates of the competing, undesired RWGS reaction.

## Conflicts of interest

The authors declare that there is no conflict of interest regarding the publication of this article.

## Acknowledgements

The authors thank ScopeM (ETH Zürich) for the use of their electron microscopy facilities. The Swiss-Norwegian Beamline (SNBL) at European Synchrotron Radiation Facility (ESRF, Grenoble) is acknowledged for provision of beamtime through proposal CH5410. SNBL staff members, Dr Wouter van Beek and Dr Dragos Stoian, are thanked for support during the experiment. Dr Felix Donat is acknowledged for assistance with the MCR analysis. This project has received funding from the Bundesamt für Energie (SI/500881-01) and ETH Zurich (ETH-40 17-2).

## Notes and references

1 J. H. Sinfelt and D. J. Yates, *Nat. Phys. Sci.*, 1971, **229**, 27–28.
2 R. B. Levy and M. Boudart, *Science*, 1973, **181**, 547–549.
3 S. T. Oyama, *The Chemistry of Transition Metal Carbides and Nitrides*, Springer, 1996.
4 H. H. Hwu and J. G. Chen, *Chem. Rev.*, 2005, **105**, 185–212.
5 A. M. Alexander and J. S. Hargreaves, *Chem. Soc. Rev.*, 2010, **39**, 4388–4401.
6 A. L. Stottlemyer, T. G. Kelly, Q. Meng and J. G. Chen, *Surf. Sci. Rep.*, 2012, **67**, 201–232.
7 W. F. Chen, J. T. Muckerman and E. Fujita, *Chem. Commun.*, 2013, **49**, 8896–8909.
8 Y. Ma, G. Guan, X. Hao, J. Cao and A. Abudula, *Renewable Sustainable Energy Rev.*, 2017, **75**, 1101–1129.
9 W. Wan, B. M. Tackett and J. G. Chen, *Chem. Soc. Rev.*, 2017, **46**, 1807–1823.
10 M. M. Moyer, C. Karakaya, R. J. Kee and B. G. Trewyn, *ChemCatChem*, 2017, **9**, 3090–3101.
11 R. Dronskowski, S. Kikkawa and A. Stein, *Handbook of Solid State Chemistry*, Wiley, 2017.
12 J. B. Claridge, A. P. E. York, A. J. Brungs, C. Marquez-Alvarez, J. Sloan, S. C. Tsang and M. L. H. Green, *J. Catal.*, 1998, **180**, 85–100.
13 A. J. Brungs, A. P. E. York, J. B. Claridge, C. Marquez-Alvarez and M. L. H. Green, *Catal. Lett.*, 2000, **70**, 117–122.
14 I. Lezcano-Gonzalez, R. Oord, M. Rovezzi, P. Glatzel, S. W. Botchway, B. M. Weckhuysen and A. M. Beale, *Angew. Chem., Int. Ed.*, 2016, **55**, 5215–5219.
15 N. Kosinov, F. J. A. G. Coumans, E. A. Uslamin, A. S. G. Wijpkema, B. Mezari and E. J. M. Hensen, *ACS Catal.*, 2016, **7**, 520–529.
16 J. Patt, D. J. Moon, C. Phillips and L. Thompson, *Catal. Lett.*, 2000, **65**, 193–195.
17 P. Liu and J. A. Rodriguez, *J. Phys. Chem. B*, 2006, **110**, 19418–19425.
18 E. B. Deeva, A. Kurlov, P. M. Abdala, D. Lebedev, S. M. Kim, C. P. Gordon, A. Tsoukalou, A. Fedorov and C. R. Müller, *Chem. Mater.*, 2019, **31**, 4505–4513.
19 W.-S. Lee, A. Kumar, Z. Wang and A. Bhan, *ACS Catal.*, 2015, **5**, 4104–4114.
20 J. A. Schaidle, J. Blackburn, C. A. Farberow, C. Nash, K. X. Steirer, J. Clark, D. J. Robichaud and D. A. Ruddy, *ACS Catal.*, 2016, **6**, 1181–1197.
21 M. M. Sullivan, C.-J. Chen and A. Bhan, *Catal. Sci. Technol.*, 2016, **6**, 602–616.
22 H. Wang, S. Liu and K. J. Smith, *Energy Fuels*, 2016, **30**, 6039–6049.
23 D. Pakhare and J. Spivey, *Chem. Soc. Rev.*, 2014, **43**, 7813–7837.
24 M. D. Porosoff, X. Yang, J. A. Boscoboinik and J. G. Chen, *Angew. Chem., Int. Ed.*, 2014, **53**, 6705–6709.
25 W. Xu, P. J. Ramirez, D. Stacchiola and J. A. Rodriguez, *Catal. Lett.*, 2014, **144**, 1418–1424.
26 S. Posada-Pérez, P. J. Ramírez, R. A. Gutiérrez, D. J. Stacchiola, F. Viñes, P. Liu, F. Illas and J. A. Rodriguez, *Catal. Sci. Technol.*, 2016, **6**, 6766–6777.
27 M. C. J. Bradford and M. A. Vannice, *J. Catal.*, 1999, **183**, 69–75.
28 J. Kehres, J. G. Jakobsen, J. W. Andreasen, J. B. Wagner, H. Liu, A. Molenbroek, J. Sehested, I. Chorkendorff and T. Vegge, *J. Phys. Chem. C*, 2012, **116**, 21407–21415.
29 D. C. LaMont, A. J. Gilligan, A. R. S. Darujati, A. S. Chellappa and W. J. Thomson, *Appl. Catal., A*, 2003, **255**, 239–253.
30 T.-c. Xiao, A. Hanif, A. P. E. York, Y. Nishizaka and M. L. H. Green, *Phys. Chem. Chem. Phys.*, 2002, **4**, 4549–4554.
31 A. P. E. York, J. B. Claridge, A. J. Brungs, S. C. Tsang and M. L. H. Green, *Chem. Commun.*, 1997, **1**, 39–40.
32 D. C. LaMont and W. J. Thomson, *Chem. Eng. Sci.*, 2005, **60**, 3553–3559.
33 P. Liang, H. Gao, Z. Yao, R. Jia, Y. Shi, Y. Sun, Q. Fan and H. Wang, *Catal. Sci. Technol.*, 2017, **7**, 3312–3324.
34 T. Xiao, H. Wang, J. Da, K. S. Coleman and M. L. H. Green, *J. Catal.*, 2002, **211**, 183–191.
35 M. M. Sullivan and A. Bhan, *J. Catal.*, 2018, **357**, 195–205.
36 J. S. Lee, S. T. Oyama and M. Boudart, *J. Catal.*, 1987, **106**, 125–133.
37 S. Chaudhury, S. K. Mukerjee, V. N. Vaidya and V. Venugopal, *J. Alloys Compd.*, 1997, **261**, 105–113.

38 H. M. Wang, X. H. Wang, M. H. Zhang, X. Y. Du, W. Li and K. Y. Tao, *Chem. Mater.*, 2007, **19**, 1801–1807.
39 E. Ochoa, D. Torres, R. Moreira, J. L. Pinilla and I. Suelves, *Appl. Catal., B*, 2018, **239**, 463–474.
40 A. Tsoukalou, P. M. Abdala, D. Stoian, X. Huang, M. G. Willinger, A. Fedorov and C. R. Muller, *J. Am. Chem. Soc.*, 2019, **141**, 13497–13505.
41 M. A. Naeem, P. M. Abdala, A. Armutlulu, S. M. Kim, A. Fedorov and C. R. Müller, *ACS Catal.*, 2020, **10**, 1923–1937.
42 A. Chithambararaj, N. Rajeswari Yogamalar and A. C. Bose, *Cryst. Growth Des.*, 2016, **16**, 1984–1995.
43 F. Ji, X. Ren, X. Zheng, Y. Liu, L. Pang, J. Jiang and S. Liu, *Nanoscale*, 2016, **8**, 8696–8703.
44 M.-M. Titirici, M. Antonietti and N. Baccile, *Green Chem.*, 2008, **10**, 1204–1212.
45 M. A. Naeem, A. Armutlulu, Q. Imtiaz, F. Donat, R. Schaublin, A. Kierzkowska and C. R. Muller, *Nat. Commun.*, 2018, **9**, 2408.
46 P. M. Abdala, H. Mauroy and W. van Beek, *J. Appl. Crystallogr.*, 2014, **47**, 449–457.
47 W. van Beek, O. V. Safonova, G. Wiker and H. Emerich, *Phase Transitions*, 2011, **84**, 726–732.
48 B. Ravel and M. Newville, *J. Synchrotron Radiat.*, 2005, **12**, 537–541.
49 A. Martini, E. Borfecchia, K. A. Lomachenko, I. A. Pankin, C. Negri, G. Berlier, P. Beato, H. Falsig, S. Bordiga and C. Lamberti, *Chem. Sci.*, 2017, **8**, 6836–6851.
50 J. Jaumot, A. de Juan and R. Tauler, *Chemom. Intell. Lab. Syst.*, 2015, **140**, 1–12.
51 D. Wang, D. S. Su and R. Schlögl, *Z. Anorg. Allg. Chem.*, 2004, **630**, 1007–1014.
52 L. Lajaunie, F. Boucher, R. Dessapt and P. Moreau, *Ultramicroscopy*, 2015, **149**, 1–8.
53 W. Wu, Z. Wu, C. Liang, P. Ying, Z. Feng and C. Li, *Phys. Chem. Chem. Phys.*, 2004, **6**, 5603–5608.
54 H. J. Guzmán, W. Xu, D. Stacchiola, G. Vitale, C. E. Scott, J. A. Rodríguez and P. Pereira-Almao, *Can. J. Chem.*, 2013, **91**, 573–582.
55 G. Vitale, H. Guzmán, M. L. Frauwallner, C. E. Scott and P. Pereira-Almao, *Catal. Today*, 2015, **250**, 123–133.
56 W. F. Chen, C. H. Wang, K. Sasaki, N. Marinkovic, W. Xu, J. T. Muckerman, Y. Zhu and R. R. Adzic, *Energy Environ. Sci.*, 2013, **6**, 943–951.
57 S. Takenaka, T. Tanaka, T. Funabiki and S. Yoshida, *J. Phys. Chem. B*, 1998, **102**, 2960–2969.
58 A. M. Beale and G. Sankar, *Chem. Mater.*, 2003, **15**, 146–153.
59 S. R. J. Likith, C. A. Farberow, S. Manna, A. Abdulslam, V. Stevanović, D. A. Ruddy, J. A. Schaidle, D. J. Robichaud and C. V. Ciobanu, *J. Phys. Chem. C*, 2018, **122**, 1223–1233.
60 Y. Zheng, Y. Tang, J. R. Gallagher, J. Gao, J. T. Miller, I. E. Wachs and S. G. Podkolzin, *J. Phys. Chem. C*, 2019, **123**, 22281–22292.